NJC

PAPER

View Article Online
View Journal | View Issue

Check for updates

Cite this: *New J. Chem.*, 2018, **42**, 20001

Anchoring ultrafine RhNi nanoparticles on titanium carbides/manganese oxide as an efficient catalyst for hydrogen generation from hydrous hydrazine†

Bing Yin,[a] Qingtao Wang,[b] Tong Liu *[b] and Guanhui Gao*[c]

Received 19th September 2018,
Accepted 5th November 2018

DOI: 10.1039/c8nj04766a

rsc.li/njc

The development of a cost-effective catalyst with high activity and 100% selectivity for hydrogen production from hydrous hydrazine under mild conditions is desirable for fuel cell applications. In this work, a series of RhNi/MnO_x-MXene NPs are prepared using a simple one-step wet-chemical method. The synthesized RhNi/MXene catalysts are characterized by XPS, TEM, SEM and ICP-AES. The ultrafine RhNi nanoparticles of 2.8 nm size are well dispersed on the bi-support (MnO_x-MXene) surface and avoid the aggregation of RhNi nanoparticles. This unique nanocatalytic system shows an active performance toward $N_2H_4{\cdot}H_2O$ decomposition under mild conditions. The optimized $Rh_{0.7}Ni_{0.3}$/MnO_x-MXene NPs exhibit excellent catalytic properties, and the corresponding TOF value can reach 1101.9 h^{-1} with 100% H_2 selectivity under mild conditions. The remarkable catalytic performance is attributed to the mild interactions of the bi-support to the NPs, which not only stabilizes the NPs to maintain good dispersion but also leaves sufficient surface active sites to facilitate the catalytic reaction.

Introduction

The development of a hydrogen (H_2) economy requires a simple and low-cost technology for H_2 manufacture and storage.[1–12] However, the discovery of safe and efficient H_2 storage media is still one of the biggest challenging obstacles for on-board hydrogen fuel applications.[13–19] Recently, hydrous hydrazine such as hydrazine monohydrate ($N_2H_4{\cdot}H_2O$) has been proposed as a promising candidate due to its high H_2 content of 8%, low material cost and stable liquid state at a wide range of temperature.[20–26] Moreover, its production of nitrogen (N_2) is the only byproduct besides H_2 through the reaction as represented in eqn (1). Ideally, two moles of H_2 in the absence of CO can be efficiently produced from one mole of $N_2H_4{\cdot}H_2O$, whereas the undesired reaction pathway as in eqn (2) should be avoided, because the generated NH_3 will poison the H_2 fuel cell.[27–30] Therefore, from the viewpoint of practical applications, the development of highly efficient catalysts toward $N_2H_4{\cdot}H_2O$ decomposition, which not only promote the complete decomposition of $N_2H_4{\cdot}H_2O$ but also simultaneously suppress NH_3 production, is important. Despite recent progress shows that Ni-based nanocatalysts possess high efficiency and selectivity toward $N_2H_4{\cdot}H_2O$ decomposition, their poor kinetics are below acceptable levels.[31]

$$H_2NNH_2 \rightarrow N_2 + 2H_2 \quad (1)$$

$$3H_2NNH_2 \rightarrow N_2 + 4NH_3 \quad (2)$$

Recently, it has been reported that amorphous oxide possesses high concentrations of unsaturated coordination sites, that is to say, several dangling bonds on the amorphous phase help in providing high surface area and strong metal–support interactions superior to the crystalline one.[32–34] In addition, in order to further avoid agglomeration of metallic nanocatalysts and maximize their stability, a suitable solid support is required to anchor well and disperse the active metallic nanoparticles (NPs). Graphene-like transition metal carbide (MXene, $Ti_3C_2(OH_xF_{1-x})_2$), as a promising solid support for a new nanocatalyst, has been widely investigated.[35–40] The studies show that the abundant functional groups on MXene surfaces, such as Ti–OH and Ti–F bonds, not only immobilize the nanoparticles during reduction but also improve the hydrophilicity of the resultant catalysts. Therefore, the utilization of amorphous oxide/MXenes to immobilize to Ni-based nanocatalysts might boost the kinetic rate as well as selectivity, and stability during the $N_2H_4{\cdot}H_2O$

[a] School of civil engineering, Qingdao University of Technology, Qingdao 266033, China
[b] College of Materials Science and Engineering, Qingdao University of Science and Technology, Zhengzhou Rd 53, 266000 Qingdao, China. E-mail: liutong@qust.edu.cn
[c] Paul-Drude-Institut für Festkörperelektronik, Hausvogteiplatz 5–7, 10117 Berlin, Germany. E-mail: gao@pdi-berlin.de

† Electronic supplementary information (ESI) available. See DOI: 10.1039/c8nj04766a

decomposition process. However, this has been rarely reported in the past decades.

Here, we creatively synthesize RhNi NPs supported on the bi-support MnO_x-MXene surface *via* a one-step wet-chemical approach. Interestingly, the prepared RhNi/MnO_x-MXene nanocatalysts show a high kinetic rate as well as 100% H_2 selectivity and excellent stability, which indicate that the bi-support can efficiently promote the catalytic kinetics toward the dehydrogenation of $N_2H_4{\cdot}H_2O$ in this nanocatalytic system.

Experiment

Synthesis of RhNi/MnO_x-MXene NPs

RhNi/MnO_x-MXene NPs were facilely synthesized by the co-reduction of the metal precursors and MXene. Scheme 1 shows the synthesis route to the $Rh_{0.7}Ni_{0.3}/MnO_x$-MXene nanocatalyst. In a typical experimental procedure, 100 mg MXene was dissolved in 2 mL water in a two-neck round-bottom flask (30 mL). Then, the aqueous solution containing rhodium chloride (0.042 mmol), nickel chloride (0.018 mmol) and manganese chloride (0.06 mmol) was added into the MXene solution, and the resultant mixture was kept under sonication for 3 h. Subsequently, a 0.5 mL aqueous solution of sodium borohydride ($NaBH_4$) (1.3 mol L^{-1}) was added into the resultant mixture under vigorous stirring for 2 h. Finally, the $Rh_{0.7}Ni_{0.3}/MnO_x$-MXene nanocatalyst was obtained by washing with deionized water and centrifugation. The synthesis of $Rh_{0.7}Ni_{0.3}/MnO_x$-MXene NPs with different Rh/Ni molar ratios was carried out following the above-mentioned process through adjusting the Rh/Ni molar ratio of initial metal precursors. Furthermore, to discuss the effect of MnO_x on catalytic properties, the $Rh_{0.7}Ni_{0.3}/MnO_x$-MXene NPs with different molar contents of Mn were prepared by the same method by altering the initial amount of Mn precursor. For comparison, $Rh_{0.7}Ni_{0.3}/MnO_x$-rGO, $Rh_{0.7}Ni_{0.3}/MnO_x$-XC 72R, $Rh_{0.7}Ni_{0.3}/MnO_x$-multiwalled carbon nanotubes (MNCTs, $Rh_{0.7}Ni_{0.3}/MnO_x$-MNCTs) and $Rh_{0.7}Ni_{0.3}/MnO_x$ samples were also synthesized by a similar procedure using $NaBH_4$ as the reducing agent.

Morphological, structural and compositional characterizations

Transmission electron microscopy (TEM) and high-resolution TEM (HRTEM) images were obtained using a Tecnai G2 F30 S-Twin instrument with a field emission gun operating at 200 kV.

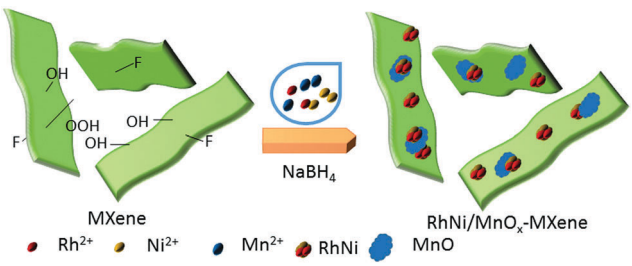

Scheme 1 Schematic representation of synthesis of the RhNi/MnO_x-MXene catalyst.

X-ray photoelectron spectroscopy (XPS) measurement was performed using an ESCALAB 250Xi spectrophotometer. The metal contents of the catalyst were analyzed using inductively coupled plasma atomic emission spectroscopy (ICP-AES) on a Leeman PROFILE SPEC. Scanning electron microscopy (SEM) and energy dispersive spectroscopy (EDS) were performed and elemental mapping images were obtained using an FEI Nova NanoSEM 450.

Results and discussion

The morphologies of pristine MXenes were characterized for the first time by scanning electron microscopy (SEM). As shown in Fig. S1 (ESI†), it can be found that pristine MXene exhibits an obvious lamellar structure with a highly rough surface. Fig. 1a–c show the typical transmission electron microscopy (TEM) and high-resolution TEM (HRTEM) images of $Rh_{0.7}Ni_{0.3}/MnO_x$-MXene hybrid. As shown in Fig. 1a and b, all the resultant RhNi NPs are highly dispersed on the surface of MnO_x-MXene with an average particle size of around 2.8 nm (Fig. S2, ESI†). The narrow size and shape distributions are mainly attributed to the 'confine effect' from the MnO_x-MXene surface, which can efficiently anchor the RhNi NPs and control their distribution during the synthesis process. The HRTEM analysis of $Rh_{0.7}Ni_{0.3}$ NPs suggests that the metallic NPs are in the crystalline state with a lattice fringe space of 0.213 nm, which differs from the fcc (111) plane of Rh (0.219 nm) and the (011) plane of Ni (0.203 nm), and thus further indicates the formation of the RhNi alloy. The real molar ratio of Rh : Ni : Mn in $Rh_{0.7}Ni_{0.3}/MnO_x$-MXene is determined to be 0.349 : 0.149 : 0.502 by inductively coupled plasma-atomic emission spectrometry (ICP-AES), which agrees well with the energy-dispersive X-ray (EDX) results (0.352 : 0.145 : 0.503).

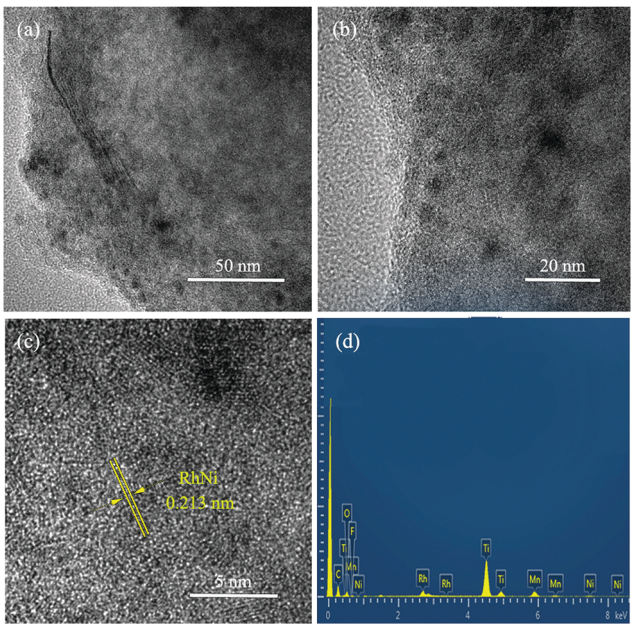

Fig. 1 TEM images (a and b), HRTEM images (c) and EDX (d) of $Rh_{0.7}Ni_{0.3}/MnO_x$-MXene.

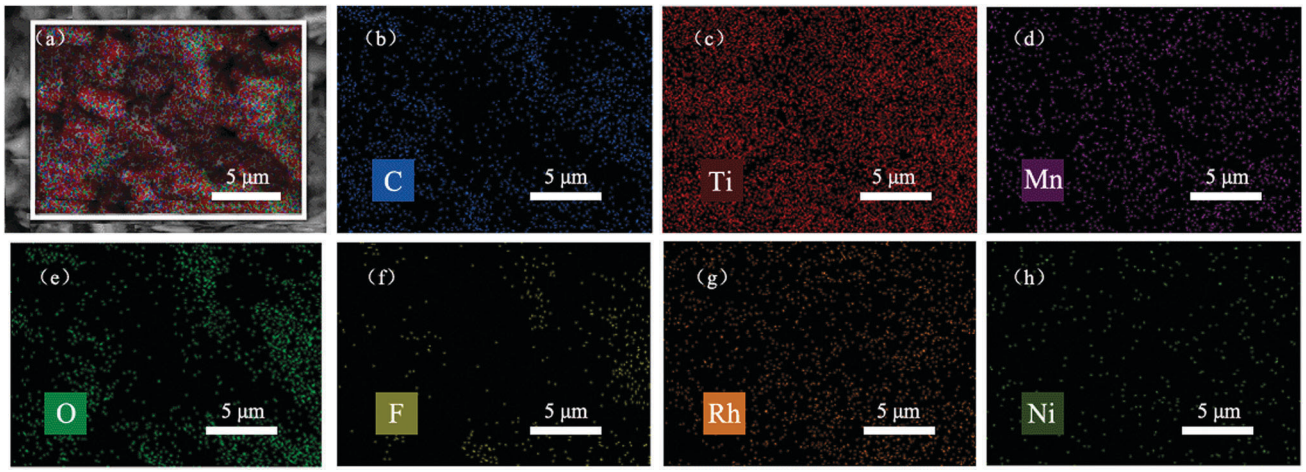

Fig. 2 The elemental mapping images of $Rh_{0.7}Ni_{0.3}/MnO_x$-MXene (a) and the corresponding elemental mapping images for C (b), Ti (c), Mn (d), O (e), F (f), Rh (g) and Ni (h).

Fig. 2 shows the elemental mapping images of the $Rh_{0.7}Ni_{0.3}/MnO_x$-MXene hybrid and the corresponding elemental mapping analysis. It can be seen that the elements of Rh and Ni are co-distributed in these NPs and homogenously dispersed on the position of C, Ti, O, F and Mn elements, further indicating the formation of RhNi and their homogeneous distribution on the surface of the MnO_x-MXene hybrid.

In order to investigate the chemical states and composition of as-prepared $Rh_{0.7}Ni_{0.3}/MnO_x$-MXene, X-ray photoelectron spectroscopy (XPS) analysis after Ar sputtering has been carried out. Fig. 3 shows the XPS spectra of RhNi/MnO_x-MXene in the survey, and individual C 1s, Ti 2p, Mn 2p, O 1s, F 1s, Rh 3d and Ni 2p regions. It can be seen from the XPS results that the C 1s spectrum can be divided into 4 peaks, which is attributed to different kinds of bonds such as C–Ti, C–C, C–OH, and HO–C═O. Additionally, the presence of F and O suggest that the functional groups such as OH and F are successfully introduced on the $Ti_3C_2X_2$ surface, which can be used as an "anchor" to enhance the hydrophilicity of the support to simultaneously facilitate the stabilization of the resultant RhNi NPs, resulting in a fine dispersion and good stability of the synthesized nanocatalyst in this heterogeneous system. The binding energies of Ni^0 $2p_{3/2}$ and Ni^0 $2p_{1/2}$ are located at 856.8 eV and 873.9 eV, respectively, which are attributed to metallic Ni^0, whereas the binding energies of Rh^0 $3d_{5/2}$ and Rh^0 $3d_{3/2}$ observed at 307.5 eV and 311.6 eV, respectively, correspond to metallic Rh^0. Moreover, the valence states of Mn in the three specimens are mainly Mn^{2+}, Mn^{3+} and Mn^{4+}. Based the above-mentioned XPS results, the synthesized RhNi/MnO_x-MXene NPs are regarded as the composition of RhNi particles supported on MnO_x-MXene. From the above-mentioned TEM and XPS results, it can be suggested that the as-synthesized RhNi NPs have been formed and well dispersed on the bi-support MnO_x-MXene surface, which will result in improving the

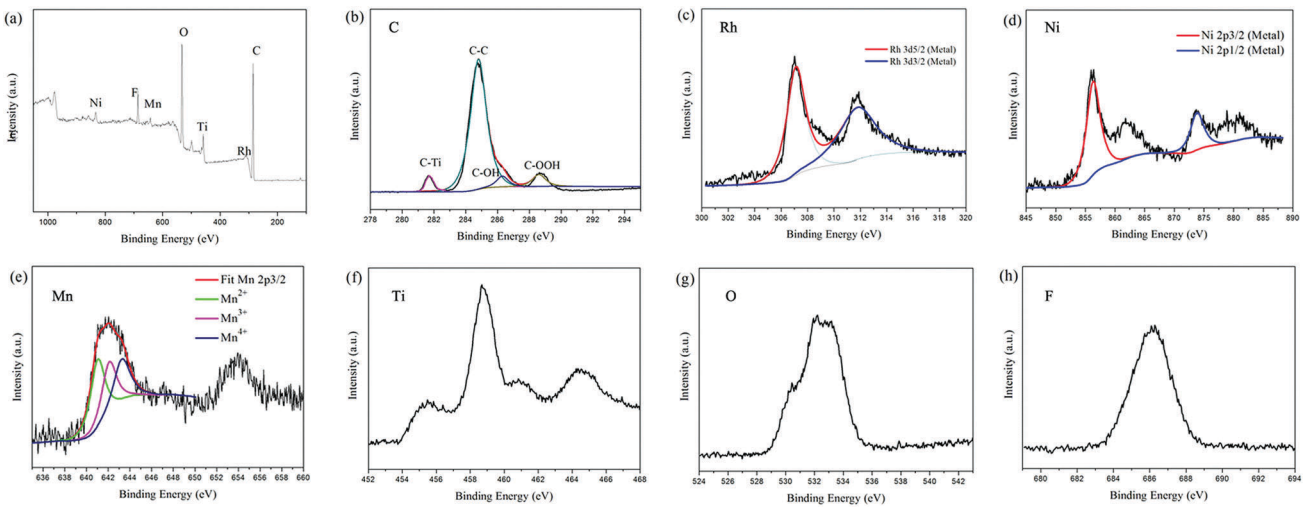

Fig. 3 Spectroscopic characteristics of $Rh_{0.7}Ni_{0.3}/MnO_x$-MXene. Survey spectrum (a), and XPS spectra of C 1s, Rh 3d, Ni 2p, Mn 2p, Ti 2p, O 1s and F 1s (b–h).

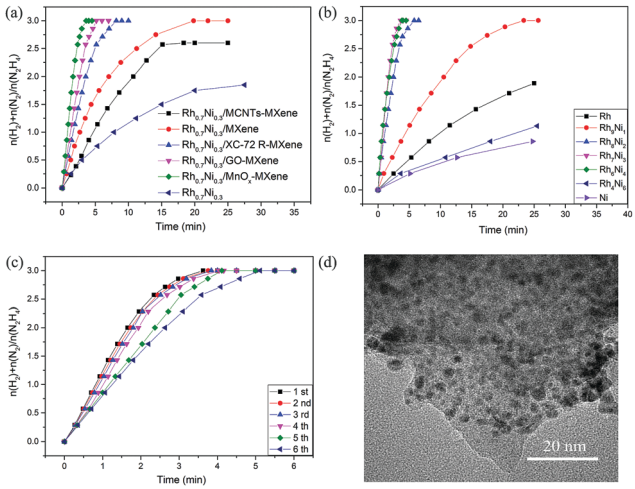

Fig. 4 Time course plots for $N_2 + H_2$ production from $N_2H_4{\cdot}H_2O$ decomposition over $Rh_{0.7}Ni_{0.3}/MnO_x$-MXene, $Rh_{0.7}Ni_{0.3}/MnO_x$-rGO, $Rh_{0.7}Ni_{0.3}/MnO_x$-XC 72R, $Rh_{0.7}Ni_{0.3}/MnO_x$-MNCTs, $Rh_{0.7}Ni_{0.3}/MnO_x$, and support-free $Rh_{0.7}Ni_{0.3}$ (a); with different Rh/Ni molar ratios (b); catalyzed by $Rh_{0.7}Ni_{0.3}/MnO_x$-MXene from 1st to 6th cycles (c); TEM image of the $Rh_{0.7}Ni_{0.3}/MnO_x$-MXene NPs after the sixth cycle (d). The molar ratio of catalyst/$N_2H_4{\cdot}H_2O$ = 0.03.

catalytic properties toward $N_2H_4{\cdot}H_2O$ decomposition in this bimetallic heterogeneous system.

The as-synthesized $Rh_{0.7}Ni_{0.3}/MnO_x$-MXene NPs have been used as catalysts for the $N_2H_4{\cdot}H_2O$ decomposition at 50 °C with a constant molar ratio of catalyst/$N_2H_4{\cdot}H_2O$ = 0.03 (Fig. 4a). For comparison, $Rh_{0.7}Ni_{0.3}/MnO_x$-rGO, $Rh_{0.7}Ni_{0.3}/MnO_x$-XC 72R, $Rh_{0.7}Ni_{0.3}/MnO_x$-MNCTs and $Rh_{0.7}Ni_{0.3}/MnO_x$ samples were also synthesized and characterized under the same conditions. Interestingly, among the above catalysts, $Rh_{0.7}Ni_{0.3}/MnO_x$-MXene exhibits the best catalytic performance. It is clear that, over the $Rh_{0.7}Ni_{0.3}/MnO_x$-MXene catalyst, 3.0 equiv. of gas ($N_2 + H_2$) can be produced in only 3.63 min with the corresponding turnover frequency (TOF) of 1101.9 h^{-1}; while over the $Rh_{0.7}Ni_{0.3}/MnO_x$-GO, $Rh_{0.7}Ni_{0.3}/MnO_x$-XC 72R, and $Rh_{0.7}Ni_{0.3}/MnO_x$ samples, the reaction can be completed between 5.2 and 19.8 min, corresponding to the TOF value of 202.1 and 769.2 h^{-1}, respectively. Even worse, $Rh_{0.7}Ni_{0.3}/MnO_x$-MNCTs can release 2.6 equiv. $N_2 + H_2$ within 25 min. The superior catalytic performance is mainly attributed to the strong interface interaction between metal and carrier, especially that the absence of MnO_x would facilitate the electron transfer between the metallic catalyst and the bi-support. The effect of MnO_x amount on the catalytic properties is investigated, and the results show that the optimum mole fraction of MnO_x is 0.5 (Fig. S3, ESI†). Increasing or decreasing this optimum value will lead to the suppression of catalytic activity.

In addition, RhNi/MnO_x-MXene nanocatalytic systems with different metal compositions are also tested toward $N_2H_4{\cdot}H_2O$ decomposition. The catalytic performance is strongly dependent on the molar ratio of Rh/Ni. Both Rh/MnO_x-MXene and Ni/MnO_x-MXene monometallic systems show certain activity toward $N_2H_4{\cdot}H_2O$ decomposition, in which 1.9 and 0.86 equiv. ($H_2 + N_2$) per $N_2H_4{\cdot}H_2O$ was released in 25 min, respectively. While for the RhNi bimetallic system, although the catalytic performance is improved with the addition of Ni, adjustment of the molar ratio of Rh : Ni to some other values will result in a change in the catalytic properties and H_2 selectivity (Fig. 4b), and thus the optimum molar ratio of Rh : Ni is determined to be 7 : 3 and the TOF value will reach 1101.9 h^{-1} with 100% H_2 selectivity. The reason for the enhanced performance of $Rh_{0.7}Ni_{0.3}$ may be mainly attributed to the synergetic effect between Rh and Ni, which can efficiently adjust the surface electronic states of bimetallic nanocatalysts, particularly related to the local strain and effective atomic coordination number at the surface, resulting in an obvious improvement for $N_2H_4{\cdot}H_2O$ decomposition.[41]

To study the effect of the OH^- group on determining the catalytic properties toward $N_2H_4{\cdot}H_2O$ decomposition, the performance of hydrogen generation from an aqueous hydrazine system with/without NaOH catalyzed by $Rh_{0.7}Ni_{0.3}/MnO_x$-MXene was further investigated. Although both samples with/without NaOH reach 100% H_2 selectivity, it should be noted that the kinetic rate of $N_2H_4{\cdot}H_2O$ decomposition could be efficiently facilitated by the addition of NaOH amount compared to that without NaOH (Fig. S4, ESI†). KOH is also used to replace NaOH, and no obvious difference is observed in the catalytic properties (Fig. S5, ESI†), which suggests that the OH^- group indeed determines the $N_2H_4{\cdot}H_2O$ decomposition.

Table 1 Catalytic activities of different catalysts for $N_2H_4{\cdot}H_2O$ decomposition

Catalyst	Solvent/medium	Temp. (°C)	Selectivity for H_2 (100%)	TOF (h^{-1})	E_a (kJ mol^{-1})	Ref.
$Rh_{0.7}Ni_{0.3}/MnO_x$-MXene	Aqueous NaOH	50	100	1101.9	36.9	This work
$Rh_{55}Ni_{45}$/Ce(OH)	Aqueous NaOH	50	100	395	38.8	47
$Rh_{34}Ni_{66}$@ZIF-8	Aqueous NaOH	50	100	140	58.1	48
$Pt_{0.6}Ni_{0.4}$/PDA-rGO	Aqueous NaOH	50	100	2056	33.39	49
$(Ni_3Pt_7)_{0.5}$–$(MnO_x)_{0.5}$/NPC-900	Aqueous NaOH	50	100	706	50.15	50
PtNi/CeO_2	Aqueous NaOH	50	100	286	38.7	51
Ni_3Pt_7/BNG-1000	Aqueous NaOH	30	100	199.4	28.4	52
$Ni_{0.9}Pt_{0.05}Rh_{0.05}/La_2O_3$	Aqueous NaOH	25	100	45.9		53
$Ni_{0.9}Pt_{0.1}/Ce_2O_3$	Aqueous NaOH	25	100	28.1	42.3	24
$Ni_{0.58}Pt_{0.42}$/graphene	Aqueous NaOH	30	100	434	23.9	54
$Ni_{0.9}P_{t0.1}$/MIL-101	Aqueous NaOH	30	100	140	48.4	55
$Rh_{0.8}Ni_{0.2}$@CeO_x/rGO	Aqueous NaOH	30	100	36.4	58	33
$(Ni_3Pt_7)_{0.5}$–$(MnO_x)_{0.5}$	Aqueous NaOH	25	100	120		56
Ni/CeO_2	Aqueous NaOH	50	100	34		57

Thanks to the optimization of NaOH promotion, the TOF increases by 3-fold (Fig. S6, ESI†), which indicates that the addition of 3 M NaOH will decrease the concentration of undesired $N_2H_5^+$ in the aqueous catalytic system. Additionally, in view of the chemical equilibrium, a strong alkaline environment will inhibit the generation of the basic NH_3 byproduct, which increases the selectivity to H_2.[42–46]

To obtain the activation energy (E_a) toward $N_2H_4{\cdot}H_2O$ decomposition catalyzed by $Rh_{0.7}Ni_{0.3}/MnO_x$-MXene catalysts, the catalytic properties at different measured temperatures (25–60 °C) were tested, and the results are presented in Fig. S6 (ESI†). The gas (N_2 + H_2) production from $N_2H_4{\cdot}H_2O$ decomposition can be finished in 2.37, 3.63, 5.33, and 14 min at 333, 323, 313, and 298 K and shows the corresponding TOF value of 1690, 1101.9, 750, and 285 h^{-1}, respectively, which is higher that the reported values in Table 1. The Arrhenius plot of ln TOF *vs.* $1/T$ for the catalyst is plotted in Fig. S6b (ESI†), and E_a is calculated to be 36.9 kJ mol^{-1}.

The durability/stability of the catalysts is the key point for commercial applications. Therefore, the durability of the $Rh_{0.7}Ni_{0.3}/MnO_x$-MXene bimetallic system up to the sixth run for $N_2H_4{\cdot}H_2O$ decomposition was carried out by adding the same amount of $N_2H_4{\cdot}H_2O$ into the catalyst after the reaction completion for the previous run. As evident from Fig. 4c, even after 6 cycles of the catalytic reaction, no apparent decrease was seen and high H_2 selectivity was still maintained well, indicating that the as-prepared $Rh_{0.7}Ni_{0.3}/MnO_x$-MXene nanocatalysts possess high durability toward $N_2H_4{\cdot}H_2O$ decomposition. It is considered that the functional OH and F groups from the $Ti_3C_2X_2$ surface, as an anchor, can efficiently stabilize the as-synthesized RhNi NPs, and avoid the aggregation of bimetallic NPs during the reaction process, which is confirmed by TEM images. As clearly seen from the TEM images (Fig. 4d), the RhNi NPs can well disperse on the MXene surface and there is no obvious aggregation of the RhNi NPs on MXene.

Conclusions

In summary, for the first time, MnO_x-MXene was used as the bi-support to prepare RhNi/MnO_x-MXene NPs for efficient hydrogen generation from $N_2H_4{\cdot}H_2O$, a promising H_2 carrier for fuel cell vehicles. The as-prepared RhNi NPs of 2.8 nm size show a fine dispersion in this heterogeneous system, which exhibit active performance toward $N_2H_4{\cdot}H_2O$ decomposition. By optimizing the fraction of Rh/Ni in a bimetallic alloy, the synthesized $Rh_{0.7}Ni_{0.3}/MnO_x$-MXene NPs have been proven to the most reactive nanocatalyst in this family for $N_2H_4{\cdot}H_2O$ decomposition and the corresponding TOF can reach 1101.9 h^{-1} with 100% H_2 selectivity, which is attributed to the strong synergetic effect between RhNi NPs and MnO_x-MXene. This work demonstrates that MnO_x-MXene is an efficient support to prepare metallic catalysts for selective H_2 production from $N_2H_4{\cdot}H_2O$ decomposition at moderate temperatures for fuel cell vehicle applications.

Conflicts of interest

There are no conflicts to declare.

Acknowledgements

This work was financially supported by the National Natural Science Foundation of China (Project No. 51303188).

Notes and references

1 X. Yang, P. Pachfule, Y. Chen, N. Tsumori and Q. Xu, *Chem. Commun.*, 2016, **52**, 4171–4174.
2 A. Kumar and Q. Xu, *ChemNanoMat*, 2018, **4**, 28–40.
3 Q. L. Zhu and Q. Xu, *Chem*, 2016, **1**, 220–245.
4 D.-J. Zhu, Y.-H. Wen, Q. Xu, Q.-L. Zhu and X.-T. Wu, *Eur. J. Inorg. Chem.*, 2017, 4808–4813.
5 Q.-L. Zhu, F.-Z. Song, Q.-J. Wang, N. Tsumori, Y. Himeda, T. Autrey and Q. Xu, *J. Mater. Chem. A*, 2018, **6**, 5544–5549.
6 Q. Sun, N. Wang, Q. Bing, R. Si, J. Liu, R. Bai, P. Zhang, M. Jia and J. Yu, *Chem*, 2017, **3**, 477–493.
7 W. Li, X. Gao, D. Xiong, F. Wei, W.-G. Song, J. Xu and L. Liu, *Adv. Energy Mater.*, 2017, **7**, 1602579.
8 C.-Y. Cao, C.-Q. Chen, W. Li, W. G. Song and W. Cai, *ChemSusChem*, 2010, **3**, 1241–1244.
9 A. Bulut, M. Yurderi, M. Kaya, M. Aydemir, A. Baysal, F. Durap and M. Zahmakiran, *New J. Chem.*, 2018, **42**, 16103–16114.
10 W. Li, X. Gao, D. Xiong, F. Xia, J. Liu, W. Song, J. Xu, S. Thalluri, M. Cerqueira, X. Fu and L. Liu, *Chem. Sci.*, 2017, **8**, 2952–2958.
11 X. Zhang, N. Shang, X. Zhou, C. Feng, S. Gao, Q. Wu, Z. Wang and C. Wang, *New J. Chem.*, 2017, **41**, 3443–3449.
12 M. R. Nabid, Y. Bide and B. Etemadi, *New J. Chem.*, 2017, **41**, 10773–10779.
13 F.-Z. Song, Q.-L. Zhu, X. Yang, W. Zhan, P. Pachfule, N. Tsumori and Q. Xu, *Adv. Energy Mater.*, 2018, **8**, 1701416.
14 Y. Du, N. Cao, L. Yang, W. Luo and G. Cheng, *New J. Chem.*, 2013, **37**, 3035–3042.
15 F.-Z. Song, Q.-L. Zhu, N. Tsumori and Q. Xu, *ACS Catal.*, 2015, **5**, 5141–5144.
16 A. E. Raevskaya, Y. V. Panasiuk, G. V. Korzhak, O. L. Stroyuk, S. Y. Kuchmiy, V. M. Dzhagan and D. T. T. Zahn, *Catal. Today*, 2017, **284**, 229–235.
17 W. Li, X. Wang, D. Xiong and L. Liu, *Int. J. Hydrogen Energy*, 2016, **41**, 9344–9354.
18 G. Nong, M. Li, Y. Y. Chen, Z. W. Zhou and S. F. Wang, *Energy*, 2016, **81**, 4712–4716.
19 F. Z. Song, Q. L. Zhu, X. C. Yang and Q. Xu, *ChemNanoMat*, 2016, **2**, 1003.
20 S. K. Singh, X. B. Zhang and Q. Xu, *J. Am. Chem. Soc.*, 2009, **131**, 9894–9895.
21 A. K. Singh and Q. Xu, *Int. J. Hydrogen Energy*, 2014, **39**, 9128–9134.
22 S. K. Singh and Q. Xu, *J. Am. Chem. Soc.*, 2009, **131**, 18032–18033.
23 J. Wang, X. B. Zhang, Z. L. Wang, L. M. Wang and Y. Zhang, *Energy Environ. Sci.*, 2012, **5**, 6885–6888.
24 H. L. Wang, J. M. Yan, Z. L. Wang, O. Song-ll and Q. Jiang, *J. Mater. Chem. A*, 2013, **1**, 14957–14962.

25 L. He, Y. Huang, A. Wang, X. Wang, X. Chen, J. J. Delgado and T. Zhang, *Angew. Chem., Int. Ed.*, 2012, **51**, 6191–6198.
26 L. He, B. L. Liang, L. Li, X. F. Yang, Y. Q. Huang, A. Q. Wang, X. D. Wang and T. Zhang, *ACS Catal.*, 2015, **5**, 1623–1628.
27 Q. L. Zhu and Q. Xu, *Energy Environ. Sci.*, 2015, **8**, 478–512.
28 H. B. Dai, Y. J. Zhong and P. Wang, *Prog. Nat. Sci.: Mater.*, 2017, **27**, 121–125.
29 K. V. Manukyan, A. Cross, S. Rouvimov, J. Millerc, A. S. Mukasyan and E. E. Wolf, *Appl. Catal., A*, 2014, **476**, 47–53.
30 P. P. Zhao, N. Cao, J. Su, W. Luo and G. Z. Cheng, *ACS Sustainable Chem. Eng.*, 2015, **3**, 1086–1093.
31 L. He, B. L. Liang, Y. Q. Huang and T. Zhang, *Natl. Sci. Rev.*, 2018, **5**, 356–364.
32 S. J. Li, H. L. Wang, B. R. Wulan, X. B. Zhang, J. M. Yan and Q. Jiang, *Adv. Energy Mater.*, 2018, 1800625.
33 Z. J. Zhang, Z. H. Lu, H. L. Tan, X. S. Chen and Q. L. Yao, *J. Mater. Chem. A*, 2015, **3**, 23520–23529.
34 J. M. Yan, Z. L. Wang, L. Gu, S. J. Li, H. L. Wang, W. T. Zheng and Q. Jiang, *Adv. Energy Mater.*, 2015, **5**, 1500107.
35 X. Xie, S. Chen, W. Ding, Y. Nie and Z. Wei, *Chem. Commun.*, 2013, **49**, 10112–10114.
36 M. Naguib, J. Come, B. Dyatkin, V. Presser, P.-L. Taberna and P. Simon, *Electrochem. Commun.*, 2012, **16**, 61–64.
37 X. Xie, Y. Xue, L. Li, S. Chen, Y. Nie, W. Ding and Z. D. Wei, *Nanoscale*, 2014, **6**, 11035–11040.
38 M. Ghidiu, M. R. Lukatskaya, M. Q. Zhao, Y. Gogotsi and M. W. Barsoum, *Nature*, 2014, **516**, 78–81.
39 M. Naguib, M. Kurtoglu, V. Presser, J. Lu, J. Niu, M. Heon, L. Hultman, Y. Gogotsi and M. W. Barsoum, *Adv. Mater.*, 2011, **23**, 4248–4253.
40 Q. Peng, J. Guo, Q. Zhang, J. Xiang, B. Liu, A. Zhou, R. Liu and Y. Tian, *J. Am. Chem. Soc.*, 2014, **136**, 4113–4116.
41 H. L. Jiang and Q. Xu, *J. Mater. Chem.*, 2011, **21**, 13705–13725.
42 X. Miao, M. M. Chen, W. Chu, P. Wu and D. G. Tong, *ACS Appl. Mater. Interfaces*, 2016, **8**, 25268–25278.
43 H. Dai, H. B. Dai, Y. J. Zhong, Q. Kang, L. X. Sun and P. Wang, *Int. J. Hydrogen Energy*, 2017, **42**, 5684–5693.
44 L. He, Y. Huang, A. Wang, Y. Liu, X. Liu, X. Chen, J. J. Delgado, X. D. Wang and T. Zhang, *J. Catal.*, 2013, **298**, 1–9.
45 C. C. Liu, J. M. Song, J. F. Zhao, H. J. Li, H. S. Qian, H. L. Niu, C. J. Mao, S. Y. Zhang and Y. H. Shen, *Appl. Catal., B*, 2012, **119–120**, 139–145.
46 H. F. Wang, L. M. Wu, A. Z. Jia, X. N. Li, Z. T. Shi, M. M. Duan and Y. J. Wang, *Chem. Eng. J.*, 2018, **332**, 637–646.
47 J. Chen, Q. Yao, J. Zhu, X. Chen and Z. H. Lu, *Int. J. Hydrogen Energy*, 2016, **41**, 3946–3954.
48 B. Q. Xia, N. Cao, H. M. Dai, J. Su, X. J. Wu, W. Luo and G. Z. Cheng, *ChemCatChem*, 2014, **6**, 2549–2552.
49 F. Z. Song, Q. L. Zhu and Q. Xu, *J. Mater. Chem. A*, 2015, **3**, 23090–23094.
50 Y. J. Ma, H. Wang, H. Li, J. L. Key, S. Ji and R. F. Wang, *RSC Adv.*, 2014, **4**, 20722–20728.
51 H. Dai, Y. P. Qiu, H. B. Dai and P. Wang, *ACS Sustainable Chem. Eng.*, 2018, **6**, 9876–9882.
52 X. Du, C. Du, P. Cai, W. Luo and G. Cheng, *ChemCatChem*, 2016, **8**, 1410–1416.
53 O. Song-ll, J. M. Yan, H. L. Wang, Z. L. Wang and Q. Jiang, *Int. J. Hydrogen Energy*, 2014, **39**, 3755–3761.
54 J. M. Chen, Z.-H. Lu, W. Huang, Z. B. Kang and X. S. Chen, *J. Alloys Compd.*, 2017, **695**, 3036–3043.
55 Z. J. Zhang, S. L. Zhang, Q. L. Yao, X. S. Chen and Z.-H. Lu, *Inorg. Chem.*, 2017, **56**, 11938–11945.
56 B. Xia, T. Liu, W. Luo and G. Cheng, *J. Mater. Chem. A*, 2016, **4**, 5616–5622.
57 W. Kang and A. Varma, *Appl. Catal., B*, 2018, **220**, 409–416.

